

CHAPTER 1

Hydrodynamical description of collective flow

Pasi Huovinen

*School of Physics and Astronomy, University of Minnesota,
Minneapolis, MN 55455, USA*

I review how hydrodynamical flow is related to the observed flow in ultrarelativistic heavy ion collisions and how initial conditions, equation of state and freeze-out temperature affect flow in hydrodynamical models.

Contents

1	Introduction	2
2	Hydrodynamical model	3
2.1	Basics	4
2.2	Initialization	5
2.3	Equation of State	9
2.4	Freeze-out	10
3	Transverse flow and its anisotropies	11
3.1	Transverse flow	12
3.2	Flow anisotropies	16
3.2.1	Directed flow	17
3.2.2	Elliptic flow	19
4	Learning from RHIC data	24
5	Summary and outlook	32
	References	34

1. Introduction

One of the goals of the experimental heavy ion program at ultrarelativistic energies is to create a dense system of strongly interacting particles. It is hoped that the particles formed in the primary collisions would rescatter often enough to reach local thermal equilibrium and behave as a particle fluid, not as a cloud of free particles. If such a state is reached, the finally observed particles should depict signs of collective behaviour such as flow.

Our intuitive understanding of flow, i.e. collective motion, is closely tied to a classical macroscopic description of flow using the language and tools of hydrodynamics. This means that it is often easiest to use hydrodynamical concepts like temperature, pressure and flow velocity to describe collective motion even if the applicability of such concepts is far from certain. Hydrodynamical models are thus particularly suitable to describe flow phenomena, but we have to be careful not to confuse what is actually observed with our way of describing observations. An example of the limits of hydrodynamical language is that there is no generally accepted definition of flow in the context of heavy-ion collisions, but the word is used in its intuitive meaning.

A rigorous definition of flow is beyond the scope of this review. Instead I use a hydrodynamically practical definition of flow: collective flow is correlation of position and momentum during the dense, interacting stage of the collision regardless of the origin of these correlations. This means that I also call flow the correlation between the longitudinal momentum and the position of particles which has its origin in the initial particle producing processes. In a hydrodynamical model these correlations are manifested as an initial non-zero longitudinal velocity field.

Unlike transverse and longitudinal flow, directed and elliptic flow do not directly refer to collective motion but to certain emission pattern where particle emission is not azimuthally isotropic (for definitions see sections 3.2.1 and 3.2.2). In principle elliptic anisotropy could be entirely due to the shape of the surface of the source and be finite even if flow the velocity is zero¹. Therefore to call elliptic anisotropy elliptic flow is unfortunate but firmly established in the literature. It has to be remembered, however, that even if elliptic anisotropy is not necessarily a sign of collective motion, it is a collective effect.

Hydrodynamics connects the conservation laws to the equation of state, viscosity and heat conductivity of the fluid. Thus the properties of matter and flow are intimately connected and we hope to learn about the equation of state of nuclear matter by studying the flow in heavy ion collisions. In practice, however, this is a challenging task because of the nonlinear nature of the equations of hydrodynamics and the many un-

knowns in the hydrodynamical description of heavy-ion collision. In this review I describe briefly the basic concepts of a hydrodynamical model and the kind of collective flow generated in hydrodynamical simulation. My emphasis is on details which have particular significance in the description of elliptic flow and how initial shape of the system, equation of state and freeze-out temperature affect elliptic flow in $Au + Au$ collisions at the Relativistic Heavy Ion Collider (RHIC) at Brookhaven National Laboratory (BNL) at $\sqrt{s} = 130$ GeV/ A energy.

The use of hydrodynamics has a long tradition in heavy ion physics. Consequently there are many previous reviews^{2,3} and introductory articles^{4,5,6} where a reader can find a more detailed discussion of hydrodynamical models. A complementary view of flow and its development in hydrodynamics is also provided in by Kolb and Heinz⁷ in this volume. Flow in heavy-ion collisions is discussed from the experimental point of view in reviews by Reisdorf and Ritter⁸ and Herrmann *et al.*⁹, although their main emphasis is in collision energies below the $\sqrt{s} = 17.2$ GeV/ A collision energy of the Super Proton Synchrotron (SPS) at CERN. These reviews also provide a discussion of the experimental detection of flow which is beyond the scope of this review.

2. Hydrodynamical model

In a hydrodynamical description a heavy ion collision is basically assumed to proceed as follows: In the initial collision a large amount of the kinetic energy of the colliding nuclei is used to create a large number of secondary particles in a small volume. These particles will subsequently collide with each other sufficiently often to reach a state of local thermal equilibrium. When the system has reached local equilibrium it is characterized by the fields of temperature, $T(x)$, chemical potentials associated with conserved charges, $\mu_i(x)$ and flow velocity, $u^\mu(x)$. The evolution of these fields is then determined by the hydrodynamical equations of motion until the system is so dilute that the assumption of local thermal equilibrium breaks down and the particles begin to behave as free particles instead.

Besides the fact that we want to be able to describe the system using a few thermodynamic variables, the hydrodynamic description has additional advantages. Hydrodynamical models are relatively simple and one essentially does not need any information other than the equilibrium equation of state of nuclear matter to solve the equations of motion. Once the equation of state and the initial state of evolution are defined, the expansion dynamics is determined and there is no need to know the details of the interaction on the microscopic level. This is especially practical when one wants to study the transition from hadronic to partonic degrees of freedom; a transition for which the details on the microscopic level are

largely unknown. The use of familiar concepts like temperature, pressure and flow velocity also leads to an intuitive and transparent picture of the evolution of the collision. The price to be paid for these advantages is a set of bold assumptions: local kinetic and chemical equilibrium and lack of dissipation. This set of assumptions may or may not be valid in such a small system as that formed in a heavy ion collision.

There is no proper proof for thermalization in heavy ion collisions. Instead, one has to revert to a heuristic comparison of collision rates of secondary particles with the lifetime of the collision system. At a temperature $T \gtrsim 200$ MeV, for example, the density of partons is $n \gtrsim 4 \text{ fm}^{-3}$ in a two flavor plasma. When the cross section is approximated by the perturbative QCD (pQCD) gluon-gluon scattering cross section of $\sigma_{gg \rightarrow gg} \approx 3$ mb, the average mean free path, $\lambda = 1/\sigma n \approx 0.8$ fm, and the time between two collisions is an order of magnitude smaller than hydrodynamically estimated lifetime of the system, $\tau = 10\text{--}20$ fm. Thus the partons should scatter several times and the system has a chance to thermalize. Another way to argue for thermalization in heavy ion collisions is simply to refer to the elliptic flow data which can be reproduced by a hydrodynamical model, but not as well by transport models¹⁰.

2.1. Basics

The equations of motion of relativistic fluid dynamics are the expressions for local conservation of energy and momentum and any conserved charge:

$$\partial_\mu T^{\mu\nu} = 0 \quad \text{and} \quad \partial_\mu j_i^\mu = 0, \quad (1)$$

where $T^{\mu\nu}$ is energy momentum tensor and j_i^μ , $i = 1, \dots, n$ are the four-currents of conserved charges. Without any additional constraints these $4 + n$ (n is the number of conserved currents) equations contain $10 + 4n$ unknown variables. The simplest and most commonly used approach to close this system of equations is the ideal fluid approximation which reduces the number of unknown variables to $5 + n$.

In the ideal fluid approximation the energy momentum tensor

$$T^{\mu\nu} = \int \frac{d^3\mathbf{p}}{(2\pi)^3 E} p^\mu p^\nu f(x, \mathbf{p}), \quad (2)$$

and currents j_i are supposed to have forms

$$T^{\mu\nu} = (\epsilon + p)u^\mu u^\nu - pg^{\mu\nu} \quad \text{and} \quad j_i^\mu = n_i u^\mu, \quad (3)$$

where ϵ , p and n_i are energy density, pressure and number density of charge i in the local rest frame of the fluid and u^μ is the flow four-velocity of the fluid. In other words all dissipative effects such as viscosity

and heat conductivity are assumed to be zero and the fluid is always in perfect local kinetic equilibrium. The additional equation needed to close the system of equations is provided by the equilibrium equation of state (EoS) of the matter, which connects the pressure to the densities: $P = P(\epsilon, n_1, \dots, n_n)$.

In principle it is possible to include small deviations from local thermal equilibrium by including dissipative effects, but in practice relativistic viscous hydrodynamics is very difficult to implement and has not yet been done⁶. For estimates of the effects of viscosity, see refs. ^{11,12}.

The numerical solution of the hydrodynamical equations of motion in all three spatial dimensions is a tedious problem. In most approaches some approximate symmetry is applied to effectively reduce the number of spatial dimensions to two or one. A trivial simplification is to assume cylindrical symmetry in the description of central collisions of spherical nuclei.

Another popular approximation is the Bjorken model¹³ where the longitudinal flow is assumed to be of the scaling form $v_z = z/t$ at all times. This requirement leads to boost invariance of the system: its pressure and energy density do not depend on the longitudinal coordinate z , if compared at the same proper time $\tau = \sqrt{t^2 - z^2}$. The solution of the equations of motion becomes independent of boosts along the beam axis and it is sufficient to solve the equations of motion in the transverse plane at $z = 0$. The obvious drawback in this approximation is that the results are independent of rapidity and one is limited to discuss only transverse behaviour. With the exception of results by Hirano *et al.*^{14,15}, the results discussed in this review are obtained in boost invariant calculations. At RHIC energies the transverse flow results at mid rapidity are very similar in both boost invariant and non-boost invariant calculations.

2.2. Initialization

Local thermal equilibrium is one of the assumptions of a hydrodynamical model, but the model itself does not specify the mechanism that leads to an equilibrated state. Since at RHIC energies the initial particle production is definitely not an adiabatic process, hydrodynamics cannot be used to describe the initial collision, but the hydrodynamical evolution must begin at a sufficient time after the initial collision when the system has had time to reach thermal equilibrium. The initial state of the system, i.e. the density distributions and flow velocities at the beginning of the hydrodynamic evolution, are not given by the model either but must be given as external input.

When analysing flow it is not enough to know what the maximum density or temperature reached in collision was. The maximum flow ve-

locity before freeze-out depends also on pressure gradient close to the edge of the system. This makes particle distributions at high p_T sensitive, not only to the maximum initial pressure, but also to the initial density profile¹⁶. The elliptic flow, on the other hand, is closely related to the initial asymmetry of the system^{17,18}. This makes choosing the initial distributions an essential part of modelling flow.

The simplest method to determine the initial state is the one proposed by Hwa and Kajantie¹⁹: Since ideal fluid expansion is isentropic and entropy is related one-to-one to the measured multiplicity at a fixed freeze-out temperature and chemical potential, the final multiplicity gives also the initial entropy of the system. Only a choice of the initial size of the system is needed to fix the (average) initial entropy density and if the equation of state is known, all other thermodynamical properties follow. This approach does not tell anything about the initial density distributions and more constraints are needed to study flow.

In boost-invariant expansion it is sufficient to specify the density profiles in the transverse plane. A plausible approach is to localize the wounded nucleon model²⁰ and assume that the density in the transverse plane is proportional to the number of participants per unit area in the transverse plane. For two nuclei colliding with impact parameter \mathbf{b} , the density of participants can be calculated from a geometric formula (ref.⁴ and references therein):

$$n_{\text{WN}}(\mathbf{s}; \mathbf{b}) = T_A(\mathbf{s} + \frac{1}{2}\mathbf{b}) \left[1 - \left(1 - \frac{\sigma_{pp} T_B(\mathbf{s} - \frac{1}{2}\mathbf{b})}{B} \right)^B \right] + T_B(\mathbf{s} - \frac{1}{2}\mathbf{b}) \left[1 - \left(1 - \frac{\sigma_{pp} T_A(\mathbf{s} + \frac{1}{2}\mathbf{b})}{A} \right)^A \right], \quad (4)$$

where σ_{pp} is the inelastic proton-proton cross section at the collision energy, T_A is the nuclear thickness function of nucleus A ;

$$T_A(\mathbf{s}) = \int_{-\infty}^{\infty} dz \rho_A(\mathbf{s}, z), \quad (5)$$

and $\rho_A(\mathbf{r})$ is nuclear density given by a Woods-Saxon distribution.

At SPS, the final particle multiplicity scales with the number of participants²¹. Thus it is natural to assume that the initial entropy density scales with the number of participants^{17,22,23} and the initial entropy density distribution is given by

$$s(\mathbf{s}; \tau_0; \mathbf{b}) = K_s(\tau_0) n_{\text{WN}}(\mathbf{s}; \mathbf{b}), \quad (6)$$

where $K_s(\tau_0)$ is a proportionality constant chosen to reproduce the observed final particle multiplicity in central collisions. This constant depends on the initial time of hydrodynamical evolution, τ_0 , which must be

chosen separately. In the following this parametrization is called sWN, as in ref. ¹⁸.

Strictly speaking the hydrodynamical approach does not allow both the transverse energy dE_T/dy and the multiplicity dN/dy to scale with the number of participants. The data, however, does not rule out the possibility that transverse energy is proportional to the number of participants ²¹. Thus one can make an assumption ^{24,25,26} that the initial energy density, not the initial entropy density, scales with the number of participants as given in Eq. (4):

$$\epsilon(\mathbf{s}; \tau_0; \mathbf{b}) = K_\epsilon(\tau_0) n_{\text{WN}}(\mathbf{s}; \mathbf{b}), \quad (7)$$

with a proportionality constant $K_\epsilon \neq K_s$. By analogy to the label sWN, this initialization is labeled as eWN.

With increasing collision energy one expects that the hard collisions between incoming partons become more and more important and finally dominate particle production ²⁷. In that limit each nucleon-nucleon collision contributes equally to the particle and energy production and the number of produced particles scales like the number of binary nucleon-nucleon collisions in the transverse plane. It is given in terms of nuclear thickness functions (Eq. (5)) as

$$n_{\text{BC}}(\mathbf{s}; \mathbf{b}) = \sigma_{pp} T_A(\mathbf{s} + \frac{1}{2}\mathbf{b}) T_B(\mathbf{s} - \frac{1}{2}\mathbf{b}). \quad (8)$$

If the system thermalizes quickly via inelastic collisions the density of produced particles defines the initial entropy density at the beginning of the hydrodynamical expansion. Thus the initial entropy density should be proportional to the number of binary collisions:

$$s(\mathbf{s}; \tau_0; \mathbf{b}) = \kappa_s(\tau_0) n_{\text{BC}}(\mathbf{s}; \mathbf{b}), \quad (9)$$

which defines parametrization sBC for initialization. The proportionality constant is now labeled κ to emphasize that its value is different from the values of K_s and K_ϵ in the sWN and eWN parametrizations.

One can also argue that each binary collision contributes equally not only to particle production but also to the energy carried by the produced particles. In that case the initial energy density should be proportional to the number of binary collisions ^{14,15}:

$$\epsilon(\mathbf{s}; \tau_0; \mathbf{b}) = \kappa_\epsilon(\tau_0) n_{\text{BC}}(\mathbf{s}; \mathbf{b}). \quad (10)$$

This parametrization is called eBC.

Each of these parametrizations leads to a different centrality dependence of the multiplicity. Thus one can use data to differentiate between them without any reference to flow. As shown in fig. 1 the multiplicity data shows slightly stronger than linear dependence on the number of

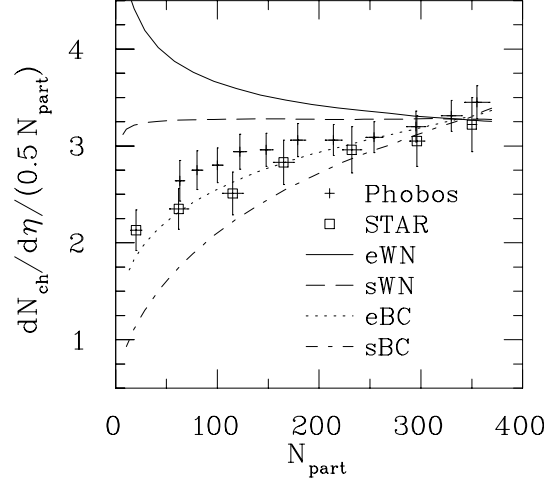


Fig. 1. Charged particle yield per participating nucleon pair at midrapidity as a function of the number of participants for different initialization models discussed in the text¹⁸. All curves were normalized to $dN_{ch}/d\eta = 550$ for 5% of the most central collisions ($b = 2.3$ fm.) The data are from refs.^{28,29}.

participants^{28,29,30}. Parametrization eBC is closest to the data, but the linear behaviour of sWN is not far from the data either. Even if the multiplicity data constrains the initial parametrization somewhat, there is still freedom in choosing a combination of these parametrizations. One should also remember that these parametrizations are not the only possibilities.

Besides the initial distributions one has to choose the initial time of hydrodynamic evolution, τ_0 . As there is no method to calculate whether the system thermalizes, there is no method to calculate when the system is sufficiently thermalized for the hydrodynamic evolution to begin. Thus the initial time is another free parameter to be chosen to fit the data or by other arguments like saturation scale in pQCD calculations. In simulations of $Au + Au$ collisions at RHIC ($\sqrt{s} = 130$ GeV), the initial time has varied from $\tau_0 = 0.2$ to 1 fm³¹.

If the assumption of boost invariance is relaxed, the choice of initial state becomes considerably more complicated. There are few constraints for the longitudinal flow velocity profile or the longitudinal density distributions. Thus the choice of a particular parametrization and the values of the parameters is largely based on trial and error – tuning the model until a reasonable fit to experimental rapidity distributions is achieved.

For a sample of initial profiles used successfully to describe longitudinal expansion at the SPS see refs. ^{32,33,34} and at RHIC refs. ^{14,34}. It is also instructive to remember that even for the same EoS there are several possible initial states which lead to an acceptable reproduction of the data ³⁵.

An alternative approach to determine the initial state is to use some other model to calculate it. For example event generator ³⁶ or perturbative QCD (pQCD) calculations ^{37,38} have been used for this purpose. Even if these approaches increase the predictive power of hydrodynamics, thermalization is still an additional assumption.

2.3. Equation of State

With the notable exception of ref. ³⁹ where the equation of state (EoS) is based on chiral SU(3) $\sigma - \omega$ model ^a all the hydrodynamical calculations at RHIC energies have used equations of state based on similar structure: a hadronic phase which is constructed as a gas of free hadrons and resonances, a plasma phase of ideal, massless partons with a bag constant and a first order phase transition between these two phases.

Different choices of the number of resonances included in the hadronic phase, of the latent heat and of the phase transition temperature cause minor differences in the equations of state of different practitioners, but the major difference is whether the hadron phase is assumed to be in chemical equilibrium or not. Thermal models used to fit final state particle abundancies give larger freeze-out temperatures $T_{ch} \sim 160$ MeV ⁴⁰ than kinetic freeze-out temperatures $T_f \sim 120$ MeV obtained from fits to particle p_T spectra. This discrepancy can be explained by different cross sections for elastic and inelastic collisions. Thermal models assume chemical equilibrium which requires frequent inelastic collisions which change particle number. On the other hand, frequent inelastic collisions are sufficient to maintain kinetic equilibrium. Since the cross sections for particle number changing collisions are much smaller than for collisions where particle number does not change (elastic and quasi-elastic collisions), it is natural to assume that inelastic collisions cease first and chemical freeze-out occurs at a higher temperature than kinetic freeze-out. Thus the system may be in local kinetic, but not chemical, equilibrium at the later stages of its evolution.

Chemical non-equilibrium can be incorporated in the hydrodynamical description by treating lowest lying hadron states as stable particles ^{41,23}. The particle number of each of these hadrons forms a con-

^aIn this paper only HBT radii were discussed and it is thus beyond the scope of this review.

served current and a finite chemical potential for each hadron is built up. Baryon and antibaryon chemical potentials are also independent in this approach. Chemical non-equilibrium changes the space-time evolution of the system only slightly because the relation between pressure and energy density is very similar both in chemical equilibrium and non-equilibrium²³. The main difference is that in chemical non-equilibrium the temperature decreases faster as energy density decreases and thus the system reaches its freeze-out temperature faster. How this changes the observed anisotropy will be discussed in section 4.

2.4. Freeze-out

At some point in the evolution the particles will begin to behave as free particles instead of a fluid and the hydrodynamical description must break down. When and where that happens is not given by hydrodynamics but must be included as external input. The conventional approach is to assume this to take place as a sudden transition from local thermal equilibrium to free streaming particles when the expansion rate of the system is larger than the collision rate between particles or the mean free path of the particles becomes larger than the system size. Finding where these conditions are fulfilled is a nontrivial problem. Since the scattering rate is strongly dependent on temperature the usual approximation assumes that the freeze-out takes place on a hypersurface where temperature (or energy density) has a chosen freeze-out value. This temperature is of the order of the pion mass, but its exact value is largely a free parameter which can be chosen to fit the data. In $Pb + Pb$ collisions at the SPS ($\sqrt{s} = 17$ GeV/ A) the calculated values of freeze-out temperatures vary between 100 and 140 MeV⁴². In $Au + Au$ collisions at RHIC ($\sqrt{s} = 130$ or 200 GeV/ A) the span of suggested freeze-out temperatures is even wider, from 100^{43,44} to 160–165 MeV^{38,45}.

After choosing the surface where the freeze-out takes place, the thermodynamic variables characterizing the state of the fluid must be converted to spectra of observable particles. A practical way of doing this is the Cooper-Frye algorithm⁴⁶ where the invariant momentum distribution of a hadron h is given by

$$E \frac{dN}{d^3p} = \frac{g_h}{(2\pi)^3} \int_{\sigma_f} \frac{1}{\exp[(p_\mu u^\mu - \mu)/T] \pm 1} p^\mu d\sigma_\mu, \quad (11)$$

where the temperature $T(x)$, chemical potential $\mu(x)$ and flow velocity $u^\mu(x)$ are the corresponding values on the decoupling surface σ_f . Besides its relative simplicity, this approach has the advantage that if the same equation of state is used on both sides of decoupling surface, both energy and momentum are conserved.

However, the Cooper-Frye formula has a conceptual problem. For those areas where the freeze-out surface is spacelike, the product $p^\mu d\sigma_\mu$ may be either positive or negative, depending on the value and direction of p^μ . In other words, the number of particles freezing out on some parts of the freeze-out surface may be negative. These negative contributions are small (a few per cent²²) and are usually ignored. More refined procedures without negative contributions have been suggested⁴⁷ but their implementation is complicated. So far there has been no full-fledged calculation using these procedures.

Another way to refine the hydrodynamical freeze-out procedure is to circumvent the entire problem and switch from a hydrodynamical to a microscopic transport model description well within the region where hydrodynamics is supposed to be applicable^{22,48}. Besides giving a better description of freeze-out, such models include the separate chemical and kinetic freeze-outs. The main drawback of such models is – besides the increased complexity – that the correct region where the switch from the hydrodynamical to the transport description should take place is as uncertain as the kinetic freeze-out surface in ordinary hydrodynamical calculation. The educated guess employed in both refs. ^{22,48} is that the switch happens immediately after hadronization.

3. Transverse flow and its anisotropies

In hydrodynamics, flow is generated by pressure gradients. In the initial state of a relativistic heavy-ion collision, there is only one type of collective motion, the coherent longitudinal motion of the two approaching nuclei. At center-of-mass energies above about 5 GeV/A nucleon pair, this initial motion can no longer be completely stopped, even for large nuclei ($A \geq 200$) undergoing fully central collisions, and a certain fraction of the collective motion in the final state is simply a remnant of the initial beam motion. To separate it from hydrodynamically generated longitudinal flow is notoriously difficult, and therefore most of the attention focuses on *transverse* collective flow in the directions perpendicular to the beam which was entirely absent before the collision and thus can be clearly associated with collective behaviour generated during the collision.

One distinguishes between transverse flow in general and its anisotropies. In some works in literature, the azimuthally averaged transverse flow is called radial flow (e.g. ref. ⁷). However, in studies of heavy ion collisions at energies around 1 GeV/A, radial flow is understood to mean three dimensional spherically symmetric flow^{8,9}. Therefore I prefer to call collective motion in the transverse plane transverse flow without any reference to its azimuthal structure. Transverse flow will be discussed in

Section 3.1.

In central ($b = 0$) collisions between spherical nuclei the transverse pressure gradients are independent of the azimuthal angle and transverse flow field is azimuthally isotropic. On the other hand in non-central ($b \neq 0$) collisions between spherical nuclei, or in central collisions between deformed nuclei (e.g. U+U), the nuclear overlap region is initially spatially deformed in the plane transverse to the beam, resulting in azimuthal anisotropies of the pressure gradients and of the final collective flow pattern generated by them. Two specific forms of anisotropy of the transverse flow field are the “directed” and the “elliptic” “flows” discussed in Sections 3.2.1 and 3.2.2 below. They are characterized and measured by the first two higher order expansion coefficients in an azimuthal Fourier expansion of the final momentum spectra. These coefficients vary for different hadron species, but the hydrodynamic model relates their magnitudes in specific ways which depend on the initial and freeze-out conditions and the equation of state of the expanding matter.

3.1. *Transverse flow*

In one-fluid hydrodynamics, the concept of transverse flow is particularly simple. The pressure gradient between the dense center of the system and the ambient vacuum causes the system to expand and transverse velocity v_r of the fluid is built up. However, if one defines the system size by the location of the freeze-out surface, the transverse flow velocity is *not* the expansion velocity of the system. Since the system dilutes, freeze-out surface may move inwards even if the particle fluid flows rapidly outwards. In such a case the whole concept of expansion velocity is ambiguous.

The equation of state (EoS) is closely related to the buildup of flow: the stiffer the EoS, the larger the flow. Unfortunately many other factors affect the flow as well and therefore p_T spectra of particles constrain the EoS only weakly. Extreme cases like the ideal pion gas EoS can be excluded as too stiff^{49,50}, but even the effect of a phase transition can be compensated by changes in the initial density and freeze-out temperature³⁵. At large values of the transverse momentum, $p_T > 2\text{--}3$ GeV/c, the particle distributions are also increasingly sensitive to the details of the velocity profile and thus to the initial pressure profile. Similar calculations may reproduce the data or not depending on the choice of the initial profile¹⁶.

The experimental detection of transverse flow is much more difficult than its hydrodynamical description. Since it is not possible to detect where each particle was emitted, it is not possible to reconstruct the flow (or its absence) either. Instead one has to deduce the presence of flow indirectly by comparing p_T distributions of various particle species. In the experimental literature the following procedure is often used to

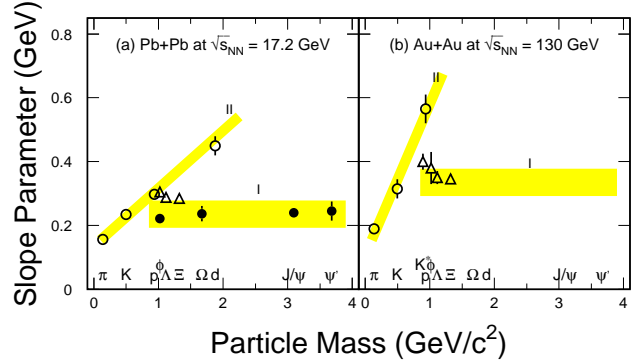


Fig. 2. Slope parameters as a function of particle mass for (a) Pb+Pb central collisions at the SPS ($\sqrt{s} = 17.2$ GeV/A) and (b) Au+Au central collisions at RHIC ($\sqrt{s} = 130$ GeV/A). From ref.⁵³.

argue for collective flow: To characterize the slope of the p_T distribution the transverse mass spectra at midrapidity can be fitted to a simple Boltzmann distribution

$$\frac{dN}{dy m_T dm_T} \propto \exp\left(-\frac{m_T}{T_{\text{slope}}}\right). \quad (12)$$

Here T_{slope} is the inverse slope parameter, often interpreted as the apparent temperature of the source. In $p + p$ collisions at 450 GeV/c⁵¹ the spectra of different particles (e.g. π , K, p) have a characteristic inverse slope parameter of about 140 MeV. On the other hand, as shown in Fig. 2, in $Pb + Pb$ collisions at the SPS⁵² and in $Au + Au$ collisions at RHIC⁵³ the slope parameter of π , K and p increases with particle mass and collision energy. The linear increase in particle mass has been interpreted as a sign that T_{slope} consists of two components: (a) thermal part, T_{therm} , associated with random motion, and (b) a part resembling collective motion with average transverse flow velocity $\langle v_r \rangle$. Both contributions can be added and give rise to the slope parameter⁵²

$$T_{\text{slope}} = T_{\text{therm}} + m \langle v_r \rangle^2. \quad (13)$$

However, one must warn against a too simpleminded use of this procedure and interpretation of Eq. (13). First of all the experimental distributions as well as the distributions given by Eqs. (11,14) are invariant

distributions whereas the thermal distribution used in the fits of Eq. (12) is not. The m_T factor required to make the distribution invariant and the integrations over the source leading to Bessel functions instead of exponentials cause the value of the slope parameter to depend on the p_T interval where the fit is carried out.

To illustrate the emission from a boosted thermal source we use the “blast-wave” model of Siemens and Rasmussen⁵⁴ where thermalized matter of temperature T_f , approximated by a boosted Boltzmann distribution, freezes out on a thin cylindrical shell. Assuming a boost-invariant longitudinal expansion, a transverse flow rapidity ρ on the shell and a freeze-out at constant proper time τ , the Cooper-Frye freeze-out distribution (Eq. (11)) can be calculated analytically^{55,56}. Up to irrelevant constants one finds

$$\frac{dN}{dy m_T dm_T} \propto m_T I_0 \left(\frac{p_T \sinh \rho}{T_f} \right) K_1 \left(\frac{m_T \cosh \rho}{T_f} \right), \quad (14)$$

where $\rho = \tanh^{-1} v_r$ is the transverse flow rapidity. The slope parameter T_{slope} is given by⁵⁷

$$\begin{aligned} \frac{-1}{T_{\text{slope}}} &= \tilde{T} = \frac{d}{dm_T} \ln \left(\frac{dN}{dy m_T dm_T} \right) \\ &\approx \frac{1}{m_T} + \frac{m_T}{p_T} \frac{\sinh \rho}{T} - \frac{\cosh \rho}{T}, \end{aligned} \quad (15)$$

where we have approximated the Bessel functions by exponentials. The slope parameter now has a much more complicated dependence on mass than the linear dependence of Eq. (13). As seen by differentiating Eq. (15) with respect to mass,

$$\frac{dT_{\text{slope}}}{dm} = \frac{1}{\tilde{T}^2} \left(-\frac{m}{m_T^3} + \frac{m}{m_T p_T} \frac{\sinh \rho}{T} \right), \quad (16)$$

there may even be a p_T -range where the slope parameter decreases as a function of mass. In a more realistic calculation the emission takes place on a surface where the flow velocity varies, and to find a p_T region where the slope parameter decreases with increasing mass requires a very large average flow velocity. At SPS and RHIC energies the flow velocity is not sufficiently large, but the slope parameters show a similar non-linear mass and p_T dependence to that depicted in Eq. (15) nevertheless.

Besides the actual properties of boosted thermal distributions, there is another complication in extracting flow velocity from the p_T distributions. A large number of detected particles do not originate from a thermal source but from resonance decays. Due to the available phase space, the decays contribute mainly to the low- p_T region leading to steeper

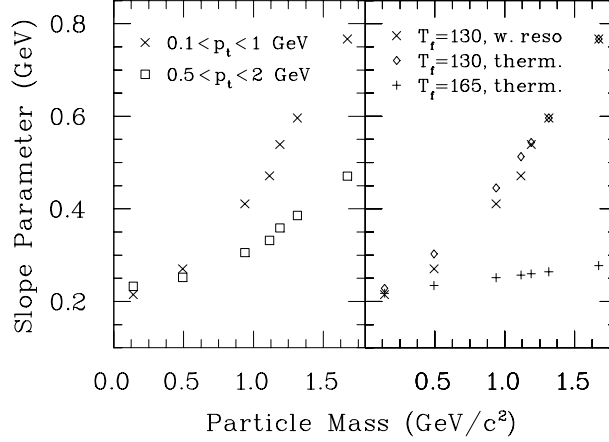


Fig. 3. Hydrodynamically calculated slope parameters as a function of particle mass in central collisions at RHIC ($\sqrt{s} = 130$ GeV/ A). In the left panel the slope parameters are from fits to spectra in two different p_T intervals. In the right panel the fits are done in interval $0.1 < p_T < 1$ GeV/ c for spectra after resonance decays (w.reso), before resonance decays (therm) and for thermal spectra immediately after hadronization at $T_c = 165$ MeV.

slopes than in the original thermal distribution. In ref. ⁵⁷ the slope parameter of daughter particles originating in two body decays was approximately related to the slope parameter of the resonance by

$$T_{\text{eff}} = \frac{p^*}{m_R} T_R, \quad (17)$$

where p^* , m_R and T_R are the momentum of the daughter particle in the rest frame of the resonance, the mass of resonance and the slope parameter of the resonance, respectively. How much the decays change the observed slope parameter depends on the particular resonance and particle species and the temperature where the yields of resonances and particles are fixed. The calculation of the spectrum of resonance products is generally a complex task and must be carried out numerically. A detailed discussion of decay kinematics is beyond the scope of this article and an interested reader is referred to refs. ^{57,58,59,60} where different aspects of resonance decays have been discussed.

How the fit intervals and resonance decays affect slope parameters can be seen in fig. 3 where hydrodynamically calculated slope parameters are shown. The calculation was tuned to reproduce the observed π and p spectra in the most central Au+Au collisions at $\sqrt{s} = 130$ GeV/ A

energy at RHIC ¹⁰. The slope parameters in the left panel are from fits to the same spectra after resonance decays at freeze-out temperature at $T_f = 130$ MeV, but the p_T range where the fit was carried out was either $0.1 < p_T < 1$ GeV or $0.5 < p_T < 2$ GeV. The pion and kaon slope parameters turned out to be quite independent of the fit interval, but all the heavier particles show a strong dependence on it. The slope parameters in the right panel are all obtained using the former fit interval, but the spectra either contained the contribution from resonance decays (w. reso) or were the spectra of thermally emitted particles (therm). For comparison the slope parameters were also calculated for thermal spectra ($T_f=165$, therm) immediately after hadronization at $T_c = 165$ MeV. As explained, the resonance contribution makes the slopes steeper and decreases the slope parameter. This effect is small for heavy particles ($m > m_\Lambda$) because there are very few resonances decaying into those particles. For the same reason, the mass dependence of the slope parameter has a jump between the Λ and Σ masses.

As seen in fig. 2 the experimental slope parameters of some particles do not follow the behaviour suggested by π , K and p . This has been used to argue that ϕ , Ω and J/Ψ do not experience flow in the same way as pions and protons, but decouple earlier ⁵³. Since the scattering cross sections of ϕ -mesons and Ω -baryons are smaller than pions and protons, this is possible, but as explained before, slope parameters are very sensitive to the p_T interval of the fit and thus not very reliable. In their recent analysis ⁶¹ the NA49 collaboration was able to fit the p_T spectra of all particles using the blast wave model (Eq. 14) and the *same* parameters for all particles including Ω and $\bar{\Omega}$. Thus the experimental situation is unclear as to whether all hadrons experience a similar flow or not.

Nevertheless, the almost mass independent slope parameters shown in fig. 2 do not imply absence of flow. To illustrate this we show the slope parameters calculated from particle distributions immediately after hadronization in fig. 3. Even if there is flow at that time, the slope parameters show only a weak dependence on mass because the average flow velocity is small (0.2 vs. 0.44 at the end of hadronic phase) and the slope parameters are dominated by the large temperature.

3.2. Flow anisotropies

The anisotropy of transverse flow is manifested as azimuthally anisotropic final particle distribution. To quantify this anisotropy, the particle spectra are expanded in harmonics of the azimuthal angle ϕ event by event ⁶²

$$\frac{dN}{dyd\phi_p} = \frac{dN}{2\pi dy} (1 + 2v_1 \cos(\phi - \phi_R) + 2v_2 \cos 2(\phi - \phi_R) + \dots),$$

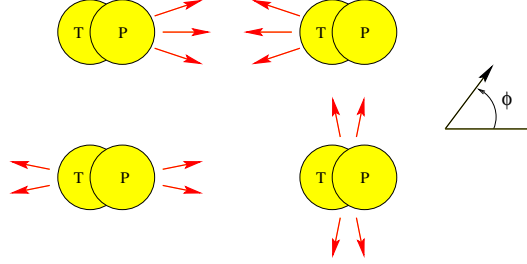


Fig. 4. Schematic representation of the collision geometry and different anisotropies of flow seen in the transverse plane. P and T denote the projectile and target nuclei, respectively. Top: directed flow in projectile rapidity region, positive (left) and negative (right). Bottom: elliptic flow, in plane (left) and out of plane (right). From ref.⁶³.

$$\frac{dN}{dydp_Td\phi_p} = \frac{dN}{2\pi dydp_T} (1 + 2v_1(p_T) \cos(\phi - \phi_R) + 2v_2(p_T) \cos 2(\phi - \phi_R) + \dots), \quad (18)$$

where ϕ_R is the azimuthal angle of the reaction plane. Assuming that the experimental uncertainties in event plane reconstruction can be corrected for, each event can be rotated such that $\phi_R = 0$. The expansion parameters v_1 and v_2 correspond to *directed* and *elliptic* flow, respectively. Due to symmetry both vanish in central collisions which are cylindrically symmetric. In symmetric collision systems the odd coefficients v_1, v_3, \dots , are zero at midrapidity.

3.2.1. Directed flow

At AGS energies the general picture of the origin of directed flow⁹ is that the pressure formed in the collision region deflects the projectile and intermediate rapidity fragments, i.e. spectator nucleons away from the target (“bounce-off” and “sidesplash” effects⁶⁴) resulting in a preferred direction of nucleon emission. Simultaneously the produced pions scatter from spectator nucleons forming resonances. Through this process the initial direction of pions is lost and flow into the direction of spectator matter is reduced. Thus pions show flow to the opposite direction than nucleons. The usual sign convention is to choose protons to have positive directed flow in the projectile rapidity region and negative in the target rapidity region. Directed flow is zero at midrapidity due to symmetry and saturates before projectile and target rapidities are reached forming an overall s-shaped curve as function of rapidity⁹.

The strength of directed flow depends on the pressure formed in the

collision region and the time that the secondary particles have to interact with the spectators, i.e. how fast the spectators pass by the collision zone. This time gets smaller with increasing energy and one expects the directed flow at SPS be smaller than at AGS, as is observed⁹. The formation of directed flow in the very early stages of the collision in very short times poses a problem for the hydrodynamical calculation. Especially at SPS and RHIC energies it is possible that most of directed flow is established before the system has reached local thermal equilibrium and the pre-equilibrium features dominate⁶⁵.

So far there are no detailed hydrodynamic calculations of directed flow at SPS or RHIC energies. However, it has been predicted that a phase transition in a nuclear equation of state would lead to a local minimum of directed flow as a function of collision energy⁶⁶. The exact position and value of this minimum depend on the details of the model, but it should be located between the AGS and the maximum SPS energy.

Another interesting prediction is that when the collision energy increases, the rapidity dependence of directed flow would eventually have such a shape that the sign of directed flow changes three times as a function of rapidity^{67,68,69}. In refs. ⁶⁷ and ⁶⁸ this behaviour is called “antiflow” and “third flow component”, respectively, and its origin is explained by the phase transition and the initial shape of the system. The phase transition leads to an initial shape of a disk slightly tilted away from the beam axis. Thus the largest pressure gradient and the direction of fastest expansion points away from the spectator nucleons and the direction of the conventional directed flow. Close to midrapidity the emission from the collision region dominates and the particles show negative directed flow in the forward and positive in the backward rapidity region, whereas close to fragmentation regions directed flow is again due to interactions with spectator matter and has its usual sign. The initial argument of ref. ⁶⁸ was for AGS energies, but has been refined for RHIC⁷⁰.

Similar behaviour for a completely different reason is predicted in ref. ⁶⁹ where the changes of sign are predicted to happen above SPS energies independent of a phase transition. Their argument is that in non-central collisions nuclear transparency leads to an anisotropic distribution of baryon number in the initial state, which is then manifested as anisotropic particle emission: when the particle fluid expands, baryons are carried to the same side as they were at the beginning of expansion. Even if the authors do not mention it, these two approaches can be expected to have observable differences in pion directed flow: emission from a tilted disk⁷⁰ is similar for both pions and protons and both should show directed flow in the same direction close to midrapidity and in opposite directions in fragmentation regions. On the other hand, an

inhomogeneous source⁶⁹ leads to pion flow in the opposite direction to proton flow at all rapidities, or alternatively to a negligibly small directed flow of pions. From the hydrodynamical point of view, both of these approaches are possible which highlights the uncertainties in choosing the initial state of hydrodynamic evolution (section 2.2).

Unfortunately the SPS data^{71,72} does not have a large enough rapidity coverage to test these ideas. So far there is no measurement of directed flow at RHIC. Whether it is large enough to be experimentally observable remains to be seen.

3.2.2. Elliptic flow

In non-central collisions the primary particle production is azimuthally isotropic, but since the interaction region is anisotropic in space, the secondary collisions can cause the final particle distribution to be anisotropic in momentum space. As depicted in fig. 5, particles heading out of plane have on the average a longer distance to go within the dense region than particles moving in plane. Thus particles moving out of plane have a larger probability to scatter several times and change their direction than particles heading in plane. Thus the final particle distribution has more particles moving in the in plane than the out of plane direction and the Fourier coefficient v_2 in Eq. 18 is positive.

In a hydrodynamic picture the buildup of such elliptic anisotropy can be understood in terms of pressure gradients. The average pressure gradient between the center of the system and the surrounding vacuum is larger in plane than out of plane direction because the system is thinner in that direction. Consequently the collective flow velocity is larger in plane than out of plane. This leads to a larger average momentum in plane than out of plane and to more particles being emitted in the in plane than the out of plane direction.

The origin of elliptic anisotropy is thus rescatterings and the shape of the system. The asymmetry of the shape of the system is largest immediately after the collision and decreases with increasing time independently of the frequency of rescatterings. Only the speed with which the system will gain an azimuthally symmetric shape depends on how frequent the rescatterings are. Thus a large elliptic anisotropy and a large value of v_2 is taken to be a signal of abundant rescatterings in the early stage of the collision and thus a signal of early pressure buildup and thermalization^{65,10}. Since hydrodynamics assumes zero mean free path and thus infinite rescattering, it is also assumed to give the practical upper limit of elliptic anisotropy.

The relation between large v_2 and early pressure buildup is difficult to quantify because of the uncertainty of the initial time of the hydrody-

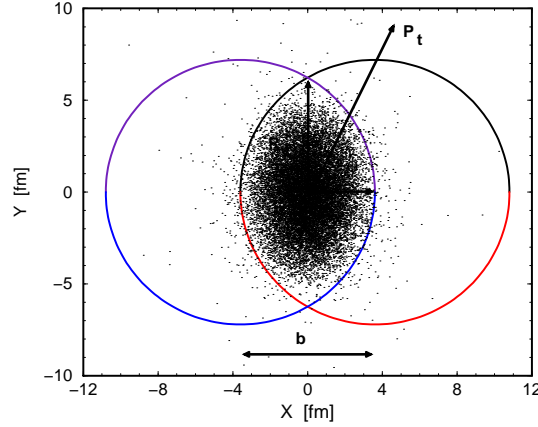


Fig. 5. Reaction plane of a semi-central $Au + Au$ collision for impact parameter $b = 7$ fm. The density of dots is proportional to the number of participating nucleons in the overlap region. From ref.⁷³.

namical evolution. If pressure buildup and thermalization take a “long” time, say several fm/c, the particles formed in the primary collisions can move significantly in the transverse plane. The geometric arguments presented in section 2.2 to constrain the initial shape are no longer valid and the initial state of hydrodynamical evolution is largely unknown. Consequently it is not possible to calculate reliably the elliptic flow parameter v_2 as function of thermalization time τ_0 . The uncertainty of shape also explains the conflicting results in the literature: if the shape does not change, v_2 is almost independent of τ_0 ¹⁷. On the other hand, if the shape changes as if the particles were freely streaming and the ratio of the anisotropy of the initial shape and the final v_2 stays the same, a delay of 3.5 fm/c in thermalization was estimated to reduce v_2 by 50%²⁴.

To gain insight how elliptic anisotropy is built up during the hydrodynamical evolution one uses so called momentum anisotropy²⁴, labeled either δ or ϵ_x in the literature,

$$\epsilon_x = \delta = \frac{\langle T^{xx} - T^{yy} \rangle}{\langle T^{xx} + T^{yy} \rangle} = \frac{\int dx dy (T^{xx} - T^{yy})}{\int dx dy (T^{xx} + T^{yy})}, \quad (19)$$

where T^{xx} and T^{yy} are the components of energy-momentum tensor $T^{\mu\nu}$, the angle brackets denote averaging over the transverse plane and

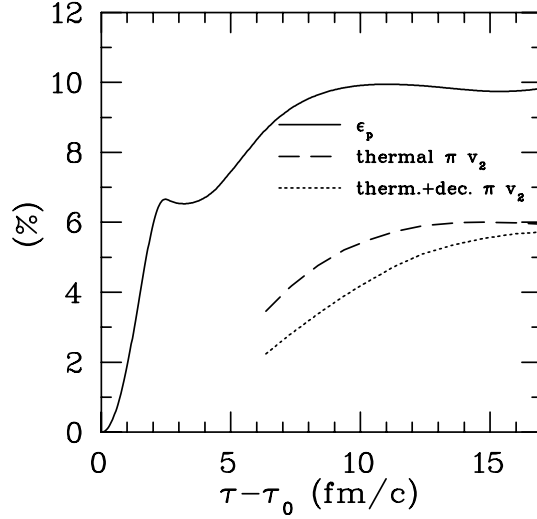


Fig. 6. Time-evolution of momentum anisotropy (solid line), elliptic anisotropy of thermal pions (dashed line) and a sum of thermal pions and pions originating from resonance decays (dotted line) in Au+Au collision at $\sqrt{s} = 130$ GeV/A with impact parameter $b = 7$ fm.

integration is done over transverse plane at constant proper time τ . As an example the time evolution of momentum anisotropy (solid line) in a simulated Au+Au collision at $\sqrt{s} = 130$ GeV/A collision energy is shown in fig. 6.

The shoulder in the increase of momentum anisotropy can be related to the phase transition²⁴. In this particular case it occurs when no part of the system is in the plasma phase anymore, but the anisotropy begins to increase before the system is entirely hadronized. As shown in ref.²⁴, the actual effect of a phase transition on the buildup of momentum anisotropy is complicated and depends on the details of the flow field at the time of the phase transition and the relative sizes of the plasma, mixed and hadronic phases at each point of time. It is possible that the increase of anisotropy is halted as in fig. 6, but it is equally possible that anisotropy keeps increasing or even decreases during the mixed phase. The decrease during the mixed phase can be explained by noting that the pressure gradients within the mixed phase are tiny and therefore the matter in the mixed phase keeps flowing with the flow velocity it had when entering the mixed phase. When the matter flows outwards with constant velocity, its flow is nearly self-similar, which decreases the

momentum anisotropy. Whether this effect can be seen in the momentum anisotropy of the *entire* system, depends on how large a part of the system is in mixed phase.

Another feature of the time evolution of the momentum anisotropy is that after saturating at $\tau - \tau_0 \approx 10$ fm, it begins to slightly decrease. This is a result of the self-cancelling nature of the anisotropy; the anisotropic pressure gradients cause the system to expand more strongly in-plane than out of plane. In the course of time the system shape becomes cylindrically isotropic, but due to momentum conservation the larger expansion in-plane continues. The system becomes elongated *in-plane* and the anisotropy of the pressure gradient begins to act against the momentum anisotropy.

The relationship between the momentum anisotropy, ϵ_p , and the observed elliptic anisotropy, v_2 , is nontrivial. The former measures the anisotropy of the collective flow velocity, whereas the latter the anisotropy of particle yield. The particle distributions are a result of both collective and thermal motion and therefore the ratio of ϵ_p and v_2 depends on the mass of the particle in question and the freeze-out temperature. To illustrate this dependence we show in fig. 6 also v_2 for pions calculated assuming freeze-out at various temperatures $165 < T_f < 90$ MeV and plotted as function of the freeze-out time of the system (dashed line). It can be seen that the momentum anisotropy increases roughly by 25% after the system is completely hadronized (at $\tau - \tau_0 \approx 6.5$ fm/c), whereas the anisotropy of pions increases by 70% – the difference caused by the increasing sensitivity of particle distributions to collective motion when temperature decreases.

Another complication in comparing the momentum anisotropy of the flow to the observed anisotropy of particle distributions are the resonance decays. The kinematics of decay not only favours the daughter particles having a smaller p_T than the decaying resonance, but also an azimuthal distribution of daughter particles which is peaked out-of-plane even if the distribution of the resonances peaks in-plane⁵⁹. This leads to daughter particles showing *negative* elliptic anisotropy, which dilutes the anisotropy of particles with thermal origin, as can be seen in fig. 6, where the dotted curve shows the v_2 of pions originating both from decays and a thermal source. The effect of resonance decays depends on temperature because the relative abundances of particles and resonances depend on temperature – the higher the temperature, the larger the fraction of pions that originates from resonance decays.

We also show the ratio ϵ_p/v_2 as function of temperature in fig. 7. It is seen that v_2 for thermal pions is roughly half of the momentum anisotropy, but when resonance decays are included, the ratio is much more temperature dependent.

In general the heavier the particle, the more sensitive it is to collec-

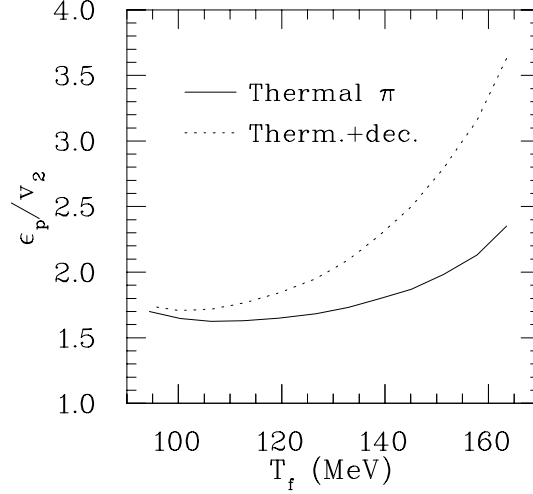


Fig. 7. The ratio of momentum anisotropy, ϵ_p , to elliptic anisotropy, v_2 , of pions as function of freeze out temperature T_f in Au+Au collisions at $\sqrt{s} = 130$ GeV/A with impact parameter $b = 7$ fm.

tive motion. For example, as explained in chapter 3.1, if the freeze-out temperature and flow velocity are the same, the heavy particles have flatter p_T distributions and thus larger slope parameters T_{slope} than lighter particles. In the same way, the p_T averaged elliptic anisotropy parameter v_2 is observed to increase with particle mass. However, at low values of p_T , the p_T -differential anisotropy parameter $v_2(p_T)$, shows the opposite behaviour: the heavier the particle, the smaller the value of $v_2(p_T)$ at fixed p_T (see fig. 8).

The apparent contradiction between v_2 and $v_2(p_T)$ has a simple explanation. v_2 is not an additive quantity, but when a p_T -averaged v_2 is calculated from $v_2(p_T)$, the latter is weighted by the particle distribution:

$$v_2 = \frac{\int dp_T v_2(p_T) \frac{dN}{dp_T}}{\int dp_T \frac{dN}{dp_T}}. \quad (20)$$

Thus the flatter p_T distribution of heavier particles weights the high p_T region, where $v_2(p_T)$ is larger, more and the p_T -averaged value can be larger. Whether this larger weight for high p_T wins over the reduction of v_2 at fixed p_T depends on the details of the expansion dynamics and the contribution from resonance decays.

The mass dependence of the elliptic anisotropy at fixed p_T can be ex-

plained as an interplay between transverse collective flow, random thermal motion and anisotropy of the flow field²⁶. It is well known that transverse flow shifts the p_T -distributions to larger values of p_T . For nonrelativistic $p_T < m$ this effect increases with the particle mass m and the transverse flow velocity $\langle v_\perp \rangle$. In the extreme case of a thin shell expanding at high velocity, the spectrum actually develops a relative minimum at $p_T = 0$ and a peak at nonzero p_T (“blast wave peak”⁵⁴), and with increasing mass the peak shifts to larger p_T . Relative to the case without transverse flow, the spectrum is thus depleted at small p_T , and the depletion, as well as the p_T range over which it occurs, increase with m and $\langle v_\perp \rangle$.

If the transverse velocity is larger in the x than the y direction, the same is true for this relative depletion effect. It counteracts the overall excess of particles moving to the x direction over particles moving to the y direction reducing v_2 . This reduction and the range where it occurs increases with particle mass and average transverse flow velocity $\langle v_\perp \rangle$. In the extreme case of a thin shell, this depletion effect can be so large that there are less small p_T particles moving in the x than the y direction, and v_2 becomes negative at low p_T . When a constant expansion velocity of a thin shell is replaced by a realistic transverse velocity distribution, the peak in the single particle spectrum disappears⁷⁴. In the same way a realistic velocity profile weakens the reduction of v_2 at low p_T , but the mass dependence of v_2 at low p_T remains. Whether particles show a positive or negative v_2 at low p_T depends on the details of the flow profile.

For relativistic $p_T > m$, the particle mass does not play a role in the thermal distribution, and consequently the curves showing $v_2(p_T)$ approach each other. In a simple model where the transverse velocity profile is replaced by its average value, as in the blast wave model of Siemens and Rasmussen⁵⁴ and its derivatives^{26,43}, v_2 increases with p_T and approaches an asymptotic value of one. The details of the velocity profile can change this behaviour, but so far hydrodynamical calculations with realistic initial conditions have shown similar monotonic increases of v_2 with p_T (see fig. 8).

4. Learning from RHIC data

One of the first measurements of $Au + Au$ reactions at the Relativistic Heavy Ion Collider (RHIC) at Brookhaven National Laboratory (BNL) at $\sqrt{s} = 130$ GeV/ A energy was a measurement of elliptic flow at midrapidity⁷⁶. Soon afterwards the elliptic flow in minimum bias collisions was shown to be very nicely reproduced by a hydrodynamical model²⁵. As shown in fig. 8, the differential anisotropy $v_2(p_T)$ in minimum bias

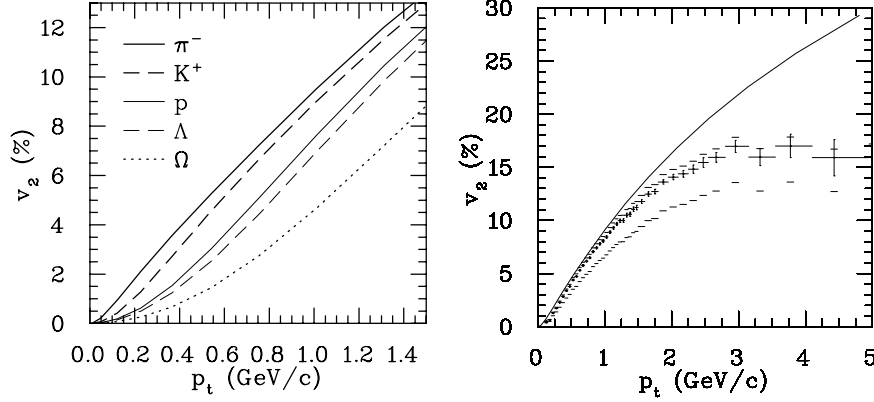


Fig. 8. The calculated p_T differential elliptic anisotropy coefficient $v_2(p_T)$ at midrapidity in minimum bias Au+Au collisions at $\sqrt{s} = 130$ GeV/A. The left figure shows $v_2(p_T)$ for various particle species²⁶ and the right figure a comparison of the calculated $v_2(p_T)$ for charged particles¹⁰ with STAR data⁷⁵.

collisions follows the hydrodynamical curve closely up to momentum $p_T = 1\text{--}1.5$ GeV. As a function of centrality the hydrodynamical description works as well or even better up to 16% of the most central collisions ($b \lesssim 6$ fm), see fig. 9. At larger impact parameters, the p_T region where the hydrodynamical calculation fits the data becomes smaller and the deviation from the hydrodynamical curve grows faster. The identified particle anisotropy shows a similar mass ordering to that discussed at the end of previous section (figs. 10 and 11), although the quantitative fit, especially of kaons, is not as good as the fit of pions and charged particles. The system thus behaves as a thermal system and this result has been taken as an indicator of thermalization¹⁰.

Since flow is closely connected to the equation of state of matter, it is possible to use details of the flow to constrain it. However, flow is equally sensitive to freeze-out temperature and the initial state of the evolution, so to learn about equation of state one must also know how flow depends on all other variables.

The basic rule as to how p_T averaged anisotropy depends on the freeze-out temperature at RHIC energies is simple. The smaller the freeze-out temperature, the larger the v_2 — if everything else in the simulation stays unchanged. This rule is not valid indefinitely. As explained in Section 3.2.2 and seen fig. 6, when the shape of the system has become azimuthally symmetric, the pressure gradients begin to work against the buildup of anisotropy and the momentum anisotropy begins to decrease. The observed v_2 may still keep increasing after the mo-

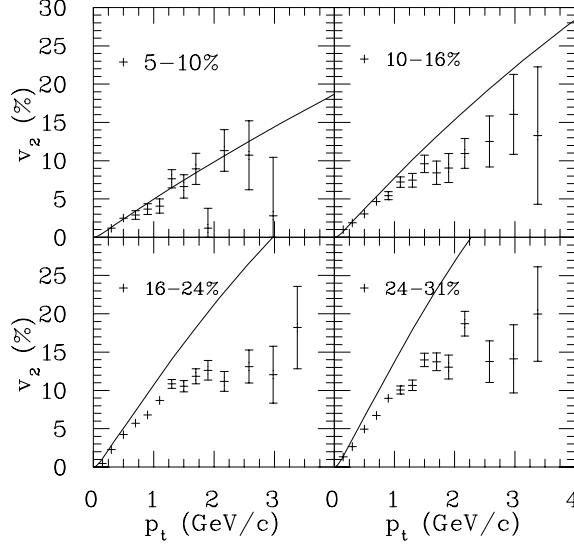


Fig. 9. The differential elliptic anisotropy $v_2(p_T)$ of charged particles in $Au + Au$ collisions at $\sqrt{s} = 130$ GeV/A at various centralities compared with the STAR data⁷⁷. The calculation is similar to that of ref.¹⁰.

mentum anisotropy has begun to decrease because lower temperature makes the final particle distributions more sensitive to the anisotropy of collective motion, but eventually it will begin to decrease too.

Unfortunately the temperature dependence of the p_T differential anisotropy, $v_2(p_T)$, is much more complicated. It is different for each particle species and it is also sensitive to the equation of state used. As shown in Fig. 11, a decrease of freeze-out temperature from 140 to 120 MeV, increases the pion $v_2(p_T)$ slightly, but decreases the proton $v_2(p_T)$. This again is a result of an interplay of collective flow and random thermal motion which is different for particles of different mass. The change in freeze-out temperature means two things: first, the lifetime of the system changes and therefore the amount of flow changes. Second the random thermal motion changes. Since the observed particle distributions are the result of both, the changes in v_2 result from both. Intuitively the effect of freeze-out temperature can be explained using the blast wave model in the same way as the mass dependence of $v_2(p_T)$ (Section 3.2.2)). When freeze-out temperature decreases, transverse flow velocity increases and the blast wave peak in the proton p_T distribution becomes more prominent and moves to larger p_T . This makes the relative depletion effect at low p_T larger and thus decreases the anisotropy.

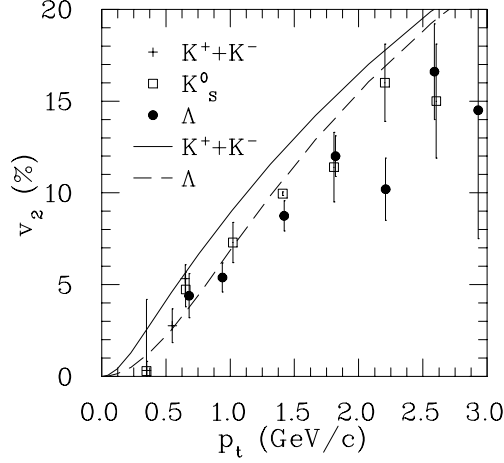


Fig. 10. The differential elliptic anisotropy $v_2(p_T)$ of kaons and Lambdas in minimum bias $Au + Au$ collisions at $\sqrt{s} = 130$ GeV/A compared with the STAR data^{43,78}. The calculation is similar to that of ref.¹⁰.

The pion p_T distribution on the other hand does not show a similar peak or it lies at very small values of p_T . Therefore there is no such depletion effect which would decrease v_2 or it is limited to very low values of p_T .

Fig. 11 also shows $v_2(p_T)$ calculated using equations of state (EoS) with a phase transition (Q) and without a phase transition (H). In both cases the change in freeze-out temperature changes $v_2(p_T)$ as described. This is not surprising since below the phase transition temperature $T_c = 165$ MeV of EoS Q, both equations of state are identical. On the other hand, if the hadronic part of the equation of state is different, a change in the freeze-out temperature may affect $v_2(p_T)$ differently. This is shown in fig. 12 where $v_2(p_T)$ for pions, kaons and protons is calculated assuming either local chemical equilibrium until kinetic freeze-out (CE), or that the relative abundancies of each particle species was frozen out immediately after phase transition at $T_{ch} = 170$ MeV (PCE). In other words, the chemical freeze-out takes place at much larger temperature than kinetic freeze-out.

In the case of chemical equilibrium (CE) the equation of state is very similar to EoS Q used to calculate the results shown in fig. 11 and the freeze-out temperature dependence is similar. The only difference is that when temperature decreases from 120 MeV to 100 MeV, the pion $v_2(p_T)$ does not increase anymore but begins to decrease. If chemical equilibrium is lost already at hadronization, the behaviour changes. The proton $v_2(p_T)$ still decreases with temperature, but the dependence is

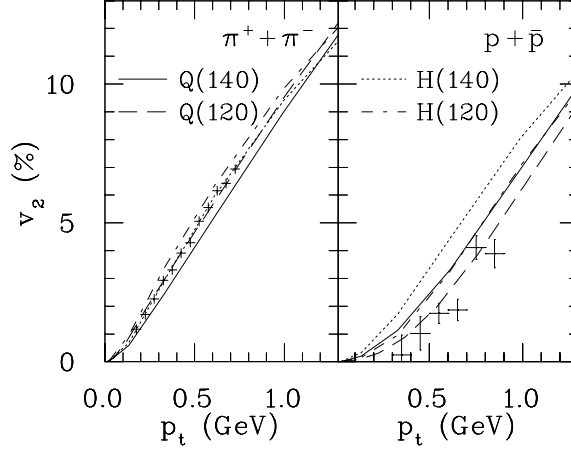


Fig. 11. The differential elliptic anisotropy $v_2(p_T)$ of pions and protons in minimum bias $Au + Au$ collisions at $\sqrt{s} = 130$ GeV/A²⁶ compared with the STAR data⁴³. The letters Q and H in the labels stand for an equation of state with a first order phase transition and a hadron gas equation of state without a phase transition, respectively. Numbers in parentheses stand for the freeze-out temperature in MeV.

much weaker. On the other hand the pion $v_2(p_T)$ increases when T_f decreases in the entire temperature interval $100 < T_f < 140$ MeV and the increase is much stronger than in the case of chemical equilibrium. The most dramatic change is in the kaon $v_2(p_T)$: if chemical equilibrium is maintained, $v_2(p_T)$ decreases when T_f decreases, but in the case of non-equilibrium, the behaviour is opposite. The kaon $v_2(p_T)$ behaves like that of pions and increases as temperature decreases. Thus there are no simple rules to tell how the observed $v_2(p_T)$ would correspond to a certain freeze-out temperature, but the constraints must be searched case by case for each equation of state.

In general a stiffer equation of state causes larger flow. This holds also for elliptic anisotropy and, at least in the case shown in fig. 11, also for p_T differential anisotropy: EoS H leads to a larger $v_2(p_T)$ for both pions and protons than EoS Q. For the chemical equilibrium or out-of-equilibrium equations of state in fig. 12 this rule is less clear because both equations of state are almost identical in both cases. The difference between CE and PCE comes from the relation between temperature and energy density. The same energy density corresponds to a smaller temperature in PCE than in CE and therefore the system cools faster. Correspondingly the flow at fixed temperature is smaller when the system is out of chemical

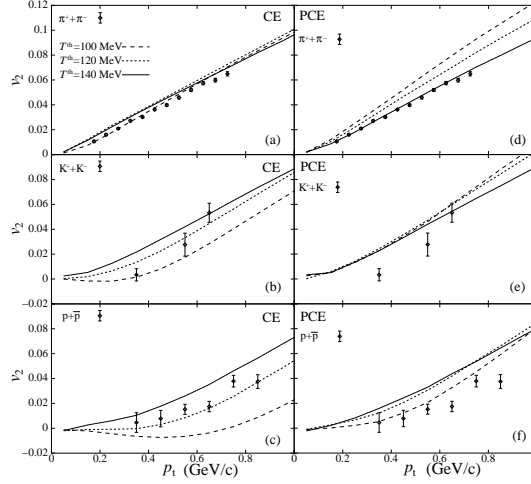


Fig. 12. The differential elliptic anisotropy $v_2(p_T)$ of pions, kaons and protons in minimum bias $Au + Au$ collisions at $\sqrt{s} = 130$ GeV/A at different kinetic freeze-out temperatures¹⁵ compared with the STAR data⁴³. The left and right panels represent the results calculated assuming local chemical equilibrium until kinetic freeze-out (CE) or chemical freeze-out already at $T_{ch} = 170$ MeV (PCE).

equilibrium and the final anisotropy looks very different in these two cases. Change to chemical non-equilibrium means ending the evolution at an earlier stage, but the effect is not as straightforward as increasing the freeze-out temperature, because the random thermal motion is not changed.

Constraining the equation of state by the transverse momentum spectra alone is notoriously difficult since larger flow generated by a stiffer equation of state can to a large extent be compensated by a higher freeze-out temperature and a slightly different initial state³⁵. As can be seen in fig. 11, essentially the same holds for pion elliptic flow: a purely hadronic equation of state (H) and an equation of state with a phase transition (Q) create similar $v_2(p_T)$ for pions if the freeze-out temperature is chosen to be $T_f = 140$ and 120 MeV for EoS H and Q, respectively. On the other hand, the effect on the proton $v_2(p_T)$ is exactly opposite: this choice leads to the largest difference of all the combinations studied. The different sensitivity of the proton and pion $v_2(p_T)$ to the equation of state and freeze-out temperature gives an additional handle on constraining both.

The results in fig. 11 clearly favour an equation of state with a phase transition. As well one could claim, based on fig. 12 that the proton

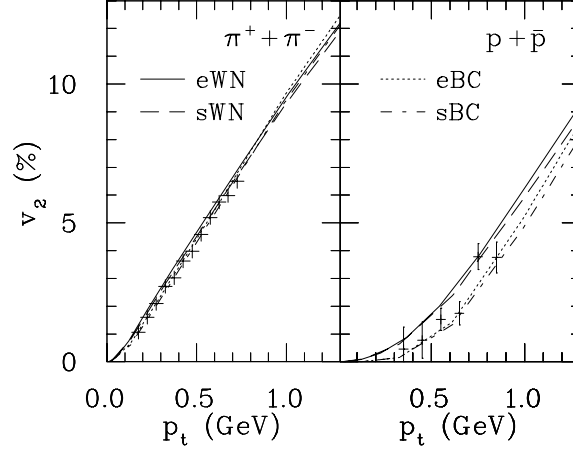


Fig. 13. The differential elliptic anisotropy $v_2(p_T)$ of pions and protons in minimum bias $Au + Au$ collisions for different initialization models¹⁸ compared with the STAR data⁴³.

$v_2(p_T)$ favours an equation of state where chemical equilibrium is maintained for temperatures lower than to $T_{ch} = 170$ MeV. Unfortunately both conclusions are premature since there are other variables to be considered which affect the observed differential anisotropy.

As explained in Section 2.2, there are various ways to parametrize the initial state of hydrodynamical evolution. The simplest ones described in Section 2.2 all lead to slightly different shapes of the initial system. If the freeze-out temperature is kept unchanged, the ratio of the initial spatial anisotropy and the observed elliptic anisotropy is almost independent of impact parameter in a hydrodynamical model^{17,24}. Despite that, the initial shape has its effect on the differential anisotropy $v_2(p_T)$ in minimum bias collisions. The anisotropy calculated using the initial state parametrizations described in Section 2.2 are shown in fig. 13¹⁸. The pion anisotropy shown in the left panel is practically independent of initialization, but the proton $v_2(p_T)$ is clearly sensitive to the initial shape. These results shown in fig. 11 were obtained using eWN initialization and in principle it is possible that combining sBC initialization with EoS H would reduce proton anisotropy sufficiently to reach the data.

The most comprehensive study of p_T spectra and anisotropies at both SPS and RHIC so far²² reached the conclusion that an equation of state with a phase transition is necessary for a consistent reproduction of the data. This study used a hybrid model of hydro and transport

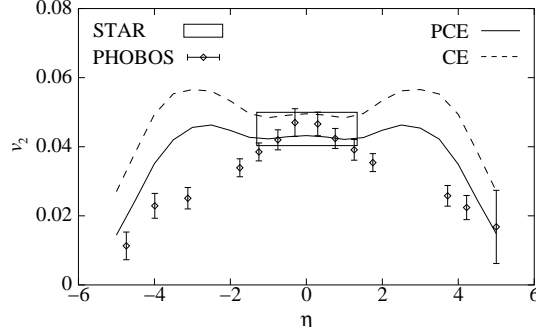


Fig. 14. Pseudorapidity dependence of elliptic anisotropy in minimum bias Au+Au collisions at $\sqrt{s} = 130$ GeV/A compared to STAR⁷⁶ and PHOBOS⁸⁰ data assuming chemical freeze out at kinetic freeze out (CE) or at hadronization (PCE)¹⁵.

where the system evolved hydrodynamically until hadronization and the hadron phase was described using a RQMD transport model. In this way the uncertainty of chemical non-equilibrium and its effects was circumvented. The freedom in initial parametrization, however, was not explored, only the initialization sWN being used. Thus in the framework of a hydrodynamical description it is safe to say so far that the data seems to favour an equation of state with a phase transition, but no final conclusion can be drawn yet.

From the hydrodynamical point of view elliptic flow at forward and backward rapidities is governed by the very same physics that creates elliptic flow at mid-rapidity. Thus to reproduce elliptic flow as a function of pseudorapidity all one has to do is to define how the initial density and shape of the system changes along the beam direction. This, however, would lead to a very counterintuitive initial shape of the system. The observed multiplicity stays approximatively constant within three units of pseudorapidity⁷⁹ which – assuming that the longitudinal flow is approximatively boost invariant – would mean that the initial entropy per unit of flow rapidity is approximatively constant within three units of rapidity. On the other hand the elliptic flow data peaks at midrapidity⁸⁰. Combined with the requirement of constant entropy, this would mean that the initial system shape is most asymmetric at midrapidity and becomes more cylindrical when fragmentation regions are approached. It is difficult to imagine a physical process leading to this kind of distribution. So far hydrodynamical calculations^{14,15} have not tried to find the initial shape to fit the data by trial and error, but have instead tried to formulate an intuitive parametrization for the initial shape and

calculated the elliptic flow based on that. These parametrizations either assume the shape not to change or to become more asymmetric towards the fragmentation regions. As a result the calculated elliptic flow fits the data only around midrapidity where $|\eta| < 1$ and stays almost constant in a large region of pseudorapidity.

There is considerable freedom in choosing the initial state in hydrodynamics and therefore it is premature to draw final conclusions as to whether the observed pseudorapidity dependence of elliptic flow really means a deviation from hydrodynamical behaviour. There may be a reasonable way to tune the initial conditions to reproduce the data which we have not thought about yet.

5. Summary and outlook

Hydrodynamical models have been surprisingly successful in explaining the flow data obtained at RHIC. The differential elliptic flow of charged particles is reproduced up to $p_T = 1.5$ GeV, its centrality dependence works below impact parameter $b \approx 6$ fm and the differential elliptic flow of identified particles shows the mass ordering predicted by hydrodynamical calculations. That a model which is based on thermal averages is able to reproduce details at the 5-10% level is remarkable. This success, however, leaves us two complementary puzzles to solve: If the system does not thermalize, why is the observed elliptic flow so close to hydrodynamical elliptic flow? Or, if the system thermalizes, what is the mechanism responsible for it and how does one describe the thermalization process? At the time of this writing, there are no answers to either of these questions.

The usefulness of flow studies and hydrodynamical models is not limited to deducing whether the collision system thermalized or not. As described in the previous chapter, flow is affected by the freeze-out temperature, the equation of state and the initial state. Thus it is possible to obtain information on all of them by studying flow, but, on the other hand, the complicated dependencies makes it challenging to constrain them individually. This requires careful simulations where one tries to reproduce as large an amount of the data as is possible and where the effects of all variables are taken into account. So far it is possible to say that the flow data favours an equation of state with a phase transition and initial state with densities well above the phase transition temperature. However, there are also open questions like the pseudorapidity dependence of flow and the HBT radii which must be solved before conclusions can be drawn.

Acknowledgements

I am indebted to many colleagues for fruitful discussions and debates. Especially I want to thank Ulrich Heinz, Peter Kolb and Denes Molnar for comments and help. This work was supported by the US Department of Energy grant DE-FG02-87ER40328.

References

1. P. Huovinen, P. F. Kolb and U. W. Heinz, Nucl. Phys. A **698**, 475 (2002) [arXiv:nucl-th/0104020].
2. H. Stocker and W. Greiner, Phys. Rept. **137**, 277 (1986).
3. R. B. Clare and D. Strottman, Phys. Rept. **141**, 177 (1986).
4. J. P. Blaizot and J. Y. Ollitrault, Adv. Ser. Direct. High Energy Phys. **6**, 393 (1990).
5. L. P. Csernai, *Introduction to relativistic heavy ion collisions*. Wiley, New York, 1994.
6. D. H. Rischke, in *Proceedings of 11th Chris Engelbrecht Summer School in Theoretical Physics : Hadrons in Dense Matter and Hadrosynthesis*, Cape Town, South Africa, Feb 4–13, 1998. Edited by J. Cleymans, H.B. Geyer, F.G. Scholtz. Berlin, Germany, Springer-Verlag, 1999. (Lecture Notes in Physics, Vol. 516) pp. 21–70 [arXiv:nucl-th/9809044].
7. P. F. Kolb and U. W. Heinz, this volume.
8. W. Reisdorf and H. G. Ritter, Ann. Rev. Nucl. Part. Sci. **47**, 663 (1997).
9. N. Herrmann, J. P. Wessels and T. Wienold, Ann. Rev. Nucl. Part. Sci. **49**, 581 (1999).
10. U. W. Heinz and P. F. Kolb, Nucl. Phys. A **702**, 269 (2002) [arXiv:hep-ph/0111075].
11. A. Muronga, Phys. Rev. Lett. **88** 062302 (2002) [Erratum-ibid. **89**, 159901 (2002)] [arXiv:nucl-th/0104064]; arXiv:nucl-th/0105046.
12. D. Teaney, arXiv:nucl-th/0301099.
13. J. D. Bjorken, Phys. Rev. D **27** (1983) 140.
14. T. Hirano, Phys. Rev. C **65**, 011901 (2002) [arXiv:nucl-th/0108004].
15. T. Hirano and K. Tsuda, Phys. Rev. C **66**, 054905 (2002) [arXiv:nucl-th/0205043].
16. A. Dumitru and D. H. Rischke, Phys. Rev. C **59**, 354 (1999) [arXiv:nucl-th/9806003].
17. J. Y. Ollitrault, Phys. Rev. D **46**, 229 (1992).
18. P. F. Kolb, U. W. Heinz, P. Huovinen, K. J. Eskola and K. Tuominen, Nucl. Phys. A **696**, 197 (2001) [arXiv:hep-ph/0103234].
19. R. C. Hwa and K. Kajantie, Phys. Rev. D **32**, 1109 (1985)
20. A. Bialas, M. Bleszynski, and W. Czyz, Nucl. Phys. **B111** (1976) 461.
21. M. M. Aggarwal *et al.* [WA98 Collaboration], Eur. Phys. J. C **18**, 651 (2001) [arXiv:nucl-ex/0008004].
22. D. Teaney, J. Lauret and E. V. Shuryak, arXiv:nucl-th/0110037.
23. D. Teaney, arXiv:nucl-th/0204023.
24. P. F. Kolb, J. Sollfrank and U. W. Heinz, Phys. Rev. C **62**, 054909 (2000) [arXiv:hep-ph/0006129].
25. P. F. Kolb, P. Huovinen, U. W. Heinz and H. Heiselberg, Phys. Lett. B **500**, 232 (2001) [arXiv:hep-ph/0012137].
26. P. Huovinen, P. F. Kolb, U. W. Heinz, P. V. Ruuskanen and S. A. Voloshin,

- Phys. Lett. B **503**, 58 (2001) [arXiv:hep-ph/0101136].
27. K. Kajantie, P.V. Landshoff, and J. Lindfors, Phys. Rev. Lett. **59** (1987) 2527; K.J. Eskola, K. Kajantie, and J. Lindfors, Nucl. Phys. **B323** 37 (1989).
 28. B. B. Back *et al.* [PHOBOS Collaboration], Phys. Rev. C **65**, 061901 (2002) [arXiv:nucl-ex/0201005].
 29. C. Adler *et al.*, Phys. Rev. Lett. **89**, 202301 (2002) [arXiv:nucl-ex/0206011].
 30. A. Bazilevsky [PHENIX Collaboration], arXiv:nucl-ex/0209025.
 31. P. Huovinen, arXiv:nucl-th/0210024.
 32. U. Ornik, M. Plumer, B. R. Schlei, D. Strottman and R. M. Weiner, Phys. Rev. C **54**, 1381 (1996) [arXiv:hep-ph/9604323].
 33. J. Sollfrank, P. Huovinen and P. V. Ruuskanen, Eur. Phys. J. C **6**, 525 (1999) [arXiv:nucl-th/9801023].
 34. K. Morita, S. Muroya, C. Nonaka and T. Hirano, Phys. Rev. C **66**, 054904 (2002) [arXiv:nucl-th/0205040].
 35. P. Huovinen, P. V. Ruuskanen and J. Sollfrank, Nucl. Phys. A **650**, 227 (1999) [arXiv:nucl-th/9807076].
 36. B. R. Schlei and D. Strottman, Phys. Rev. C **59**, 9 (1999) [arXiv:nucl-th/9806034].
 37. K. J. Eskola, P. V. Ruuskanen, S. S. Rasanen and K. Tuominen, Nucl. Phys. A **696** 715 (2001) [arXiv:hep-ph/0104010].
 38. K. J. Eskola, H. Niemi, P. V. Ruuskanen and S. S. Rasanen, arXiv:hep-ph/0206230.
 39. D. Zschesche, S. Schramm, H. Stocker and W. Greiner, Phys. Rev. C **65**, 064902 (2002) [arXiv:nucl-th/0107037].
 40. J. Cleymans and K. Redlich, Phys. Rev. C **60**, 054908 (1999) [arXiv:nucl-th/9903063].
 41. H. Bebie, P. Gerber, J. L. Goity and H. Leutwyler, Nucl. Phys. B **378** 95 (1992).
 42. D. H. Rischke, Nucl. Phys. A **698** 153 (2002) [arXiv:nucl-th/0104071].
 43. C. Adler *et al.* [STAR Collaboration], Phys. Rev. Lett. **87**, 182301 (2001) [arXiv:nucl-ex/0107003].
 44. P. F. Kolb and R. Rapp, arXiv:hep-ph/0210222.
 45. W. Broniowski and W. Florkowski, Phys. Rev. Lett. **87**, 272302 (2001) [arXiv:nucl-th/0106050].
 46. F. Cooper and G. Frye, Phys. Rev. D **10** 186 (1974).
 47. K. A. Bugaev, Nucl. Phys. A **606** 559 (1996) [arXiv:nucl-th/9906047]; K. A. Bugaev and M. I. Gorenstein, arXiv:nucl-th/9903072; V. K. Magas *et al.*, Nucl. Phys. A **661** 596 (1999) [arXiv:nucl-th/0001049].
 48. S. A. Bass and A. Dumitru, Phys. Rev. C **61** 064909 (2000) [arXiv:nucl-th/0001033].
 49. E. Schnedermann and U. W. Heinz, Phys. Rev. C **50**, 1675 (1994) [arXiv:nucl-th/9402018].
 50. J. Sollfrank, P. Huovinen, M. Kataja, P. V. Ruuskanen, M. Prakash and R. Venugopalan, Phys. Rev. C **55**, 392 (1997) [arXiv:nucl-th/9607029]

51. B. Alper *et al.* [British-Scandinavian Collaboration], Nucl. Phys. B **100**, 237 (1975); K. Guettler *et al.* [British-Scandinavian-MIT Collaboration], Nucl. Phys. B **116**, 77 (1976).
52. I. G. Bearden *et al.* [NA44 Collaboration], Phys. Rev. Lett. **78**, 2080 (1997).
53. N. Xu and M. Kaneta, Nucl. Phys. A **698**, 306 (2002) [arXiv:nucl-ex/0104021].
54. P. J. Siemens and J. O. Rasmussen, Phys. Rev. Lett. **42**, 880 (1979).
55. P. V. Ruuskanen, Acta Phys. Polon. B **18**, 551 (1987).
56. U. Heinz, K.S. Lee, and E. Schnedermann, Adv. Ser. Direct. High Energy Phys. **6**, 471 (1990).
57. E. Schnedermann, J. Sollfrank and U. W. Heinz, Phys. Rev. C **48**, 2462 (1993) [arXiv:nucl-th/9307020].
58. J. Sollfrank, P. Koch and U. W. Heinz, Z. Phys. C **52**, 593 (1991).
59. T. Hirano, Phys. Rev. Lett. **86**, 2754 (2001) [arXiv:nucl-th/0004029].
60. W. Florkowski, W. Broniowski and M. Michalec, Acta Phys. Polon. B **33**, 753 (2002) [arXiv:nucl-th/0106009].
61. S. V. Afanasiev *et al.* [NA49 Collaboration], arXiv:nucl-ex/0208014.
62. S. Voloshin and Y. Zhang, Z. Phys. C **70**, 665 (1996) [arXiv:hep-ph/9407282].
63. J. Y. Ollitrault, Nucl. Phys. A **638**, 195C (1998) [arXiv:nucl-ex/9802005].
64. H. A. Gustafsson *et al.*, Phys. Rev. Lett. **52**, 1590 (1984).
65. H. Sorge, Phys. Rev. Lett. **78**, 2309 (1997) [arXiv:nucl-th/9610026].
66. D. H. Rischke, Y. Pursun, J. A. Maruhn, H. Stocker and W. Greiner, Heavy Ion Phys. **1**, 309 (1995) [arXiv:nucl-th/9505014].
67. J. Brachmann, S. Soff, A. Dumitru, H. Stocker, J. A. Maruhn, W. Greiner and D. H. Rischke, Phys. Rev. C **61**, 024909 (2000) [arXiv:nucl-th/9908010].
68. L. P. Csernai and D. Rohrlich, Phys. Lett. B **458**, 454 (1999) [arXiv:nucl-th/9908034].
69. R. J. Snellings, H. Sorge, S. A. Voloshin, F. Q. Wang and N. Xu, Phys. Rev. Lett. **84**, 2803 (2000) [arXiv:nucl-ex/9908001].
70. V. K. Magas, L. P. Csernai and D. D. Strottman, Phys. Rev. C **64**, 014901 (2001) [arXiv:hep-ph/0010307].
71. H. Appelshauser *et al.* [NA49 Collaboration], Phys. Rev. Lett. **80**, 4136 (1998) [arXiv:nucl-ex/9711001].
72. M. M. Aggarwal *et al.* [WA98 Collaboration], arXiv:nucl-ex/9807004.
73. H. Heiselberg, private communication.
74. K. S. Lee, U. W. Heinz and E. Schnedermann, Z. Phys. C **48**, 525 (1990).
75. C. Adler *et al.* [STAR Collaboration], Phys. Rev. Lett. **90**, 032301 (2003) [arXiv:nucl-ex/0206006].
76. K. H. Ackermann *et al.* [STAR Collaboration], Phys. Rev. Lett. **86**, 402 (2001) [arXiv:nucl-ex/0009011].
77. C. Adler *et al.* [STAR Collaboration], Phys. Rev. C **66**, 034904 (2002) [arXiv:nucl-ex/0206001].
78. C. Adler *et al.* [STAR Collaboration], Phys. Rev. Lett. **89**, 132301 (2002)

- [arXiv:hep-ex/0205072].
79. B. B. Back *et al.* [PHOBOS Collaboration], Phys. Rev. Lett. **87**, 102303 (2001) [arXiv:nucl-ex/0106006].
80. B. B. Back *et al.* [PHOBOS Collaboration], Phys. Rev. Lett. **89**, 222301 (2002) [arXiv:nucl-ex/0205021].